Supplementary Material for
Learning Neural Light Transport

Paul Sanzenbacher
Autonomous Vision Group
University of Tübingen, Germany
paul.sanzenbacher@tue.mpg.de

Lars Mescheder
Amazon
Tübingen, Germany
lamesch@amazon.de

Andreas Geiger
Autonomous Vision Group
University of Tübingen, Germany
andreas.geiger@tue.mpg.de

Abstract

This supplementary document provides additional information on our approach and more experimental results. First, we provide detailed information on the Light Transport and Image Synthesis Layers in Sec. 1. We then describe the data generation pipeline in more detail in Sec. 2. Afterwards, we provide more information on the training procedure in Sec. 3, including a proof showing that we can train our models using noisy, unbiased renderings as supervision signal. Finally, we provide additional qualitative and quantitative results in Sec. 4.

1. Architectures

1.1. Light Transport Layer

The core of the Light Transport Layer is a PointNet-based architecture [9] with fully-connected ResNet blocks [2], which is illustrated in Fig. 1. While the PointNet architecture can have arbitrary depth (number of ResNet blocks), we use a depth of two for all the experiments in the paper.

Since we train our model on dynamic scenes with a variable number number of visible objects, the input point clouds have different sizes for different training samples. In theory this is not a big problem, as PointNets can handle arbitrary point cloud sizes. However, since we are using mini batches for training, having the same number of points for each training sample is desirable. Therefore, our model always operates on the maximum point cloud size, and invisible objects are masked in the architecture using per-point visibility flags.

1.2. 3D-to-2D Projection Step

In the 3D-to-2D projection step, the 3D point features are projected to image space, where the point locations are discretized. Points that are occluded by the scene's geometry are masked out, which is determined by performing an occlusion check using a rendered depth map. To make sure that we do not accidentally remove points on the scene's surface, we use a tolerance of $\varepsilon = 10^{-3}$ in the occlusion check. If multiple features are projected to the same pixel, we compute the mean feature vector for all points projecting to that pixel. If a pixel has no points projecting to it, its feature vector is defined as zero.

1.3. Image Synthesis Layer

The input to the Image Synthesis Layer are the projected features from the projection step and additional information in image space, which can be computed cheaply using OpenGL shaders These image space buffers contain information about the geometry and material information observed from the current view. They include depth map, albedo (diffuse reflectance), normal map in world coordinates as well as a view ray map, which contains for each pixel the ray direction in world coordinates going from the camera center through the respective pixel center. The intention behind using these image space layers is to leverage the image formation process in multiple ways. The normal and view direction information can be used by the network to infer shading in image space. The albedo layer supports texture synthesis where point projections are sparse. In addition, by providing this information in image space, the light transport layer can solely focus on the task of modeling the illumination in the scene. However, the image space layers do not contain useful information for reasoning about light transport in the scene. A detailed visualization and description of the Image Synthesis Layer is provided in Fig. 2.

2. Datasets

2.1. Data Generation and Sampling

The datasets used in our experiments comprise a single scene for each static scene dataset, and four scenes for dynamic experiments [1]. Since the data generation procedure for static scenes is a simplification of the dynamic case, we only describe the dynamic case in this section. Since we use learnable feature descriptors in our model, we must ensure that there are point correspondences between different training samples of the same scene. To this end, we sample an initial, static point cloud for each scene. This point cloud is then modified according to the scene modifications in the training sample. If an object is removed from the scene, the points are removed from the initial point cloud. If an object is translated, the points sampled from its surface are translated accordingly. For each scene in the dataset, we first sample a static point cloud, which is then modified for each sample in the dataset. A positive side effect of this is that we only have to store scene modification information for each sample, saving memory.

2.2. View Sampling

For each scene, we would like to cover the space of possible viewing locations and directions as accuractely as possible. At the same time we want to have a high number of views where a lot of scene details are visible to have an effective supervision signal for training. We observe that most of the objects in a scene are arranged along the walls or the floor. Therefore, we sample a viewing location uniformly from a bounding box that is slightly smaller than the scene's bounding box. Note that this means that a few of the sampled locations might lie inside an object. However, we found that these "outliers" do not pose a problem to our method in practice as long as we observe a sufficiently large number of views outside of objects during training. Next, we sample a viewing direction by sampling a look-at location uniformly from a bounding box that is half the size of the location bounding box. As a result, the distance between the camera and scene objects is far enough to render views with rich image content.

2.3. Point Cloud Sampling

We define a scene by a set of shapes $\mathcal{S}$, where each shape $S_i \in \mathcal{S}$ is itself a set of triangles. Each shape is assigned a sampling importance $w(S_i)$ corresponding to its surface area, which is the sum of triangle areas for that shape. Given the sampling importances and a point cloud of size N, we first sample N shapes according to a distribution where the probability of sampling a shape is proportional to its sampling importance. This can be achieved by using discrete inverse transform sampling, where a discrete cumulative distribution is calculated for the sequence of shapes $(S_1, \dots, S_n)$:

$$\text{cdf}(i) = \frac{\sum_{j=1}^{i} w(S_j)}{\sum_{j=1}^{n} w(S_j)} \tag{1}$$

Using a uniform sample $s \sim \mathcal{U}(0,1)$, a shape index i can be sampled according to

$$i = \arg\max_{k} \left\{ k : \text{cdf}(k) < u \right\}, \tag{2}$$

which can be implemented efficiently using bisection.

For each shape sampled from the distribution, our goal is to obtain a point sampled uniformly from the shape's surface. Since we work with a mesh scene representation, all the shapes are represented by a set of triangles. Therefore, for each point we first sample the triangle with the same technique we used for shape sampling, using the triangle area as sampling importance. Then, we sample a point location uniformly from the triangle. This way, uniformly distributed samples from the shapes' surfaces can be obtained.

2.4. Scene Modification Sampling

To train our model on all possible scene configurations (each object or light source could be located anywhere or not be present in the scene at all), we must cover this distribution well in the dataset. To this end, we manually define for each dynamic object an axis-aligned bounding box from which we sample a position for each training sample. The bounding boxes can also be limited to one or two dimensions, e.g. if an object can only be translated along a wall. Although we do not always get realistic object arrangements using this sampling strategy, this is not a limitation, as it makes our model more general (i.e. our model is trained for both realistic and non-realistic object arrangements). In addition to object translations, we randomly remove objects with a probability of 0.2 per object from the scene.

3. Training

3.1. Hyperparameters

We train all models using the Adam optimizer [4] with a learning rate of $\lambda = 5 \times 10^{-4}$, which we decay by a factor of 0.99 after each epoch. These hyperparameters are the result of a hyperparameter optimization using grid search, where we tested different learning rates and decay rates for Adam and RMSprop for 100,000 iterations. For the static scene experiment in Section 4.1 of the main paper we use a batch size of 128. For the dynamic scene experiments in Section 4.2 of the main paper we use a batch size of 32, as more GPU memory is required for the Light Transport Layer implementation. All models were created and trained using PyTorch 1.0[1] [8].

3.2. Supervised Learning with Noisy Renderings

Since rendering a large set of photorealistic renderings for training would require a lot of time, we use noisy renderings from a physically based renderer as supervision. More specifially, we use the bidirectional path tracing implementation in Mitsuba [3]. Similar techniques have recently been used to learn image denoising [7, 5]. Our key insight is that we can exploit the unbiasedness of state-of-the-art rendering algorithms like bidirectional path tracing [6] to obtain unbiased gradient estimates.

To this end, we describe the input to our network by random variable $\mathbf{X}$, which comprises a point cloud $\mathbf{P}$, a view represented by a world-to-view transform $\mathbf{T}$ and additional image-space information $\mathbf{A}$ as described in Chapter 3 of the main paper. As supervision signal, we render a noisy image $\hat{\mathbf{I}}$ that is an unbiased estimate of the ground truth rendering $\mathbf{I}(\mathbf{X})$. When we train our network using the mean squared error (MSE) and stochastic gradient descent, our gradients will be unbiased when using these noisy supervision renderings from such an unbiased rendering algorithm. Formally, this can be expressed as follows:

Lemma 1. *Let $\mathbf{X}$ be an input representation of a scene, φ_θ our rendering network and $\hat{\mathbf{I}}$ a noisy rendering of $\mathbf{X}$ following a distribution $p(\hat{\mathbf{I}}|\mathbf{X})$ which depends on the chosen sampling-based rendering algorithm. Assume that the true (noise-free) rendering is given by $\mathbf{I}(\mathbf{X})$. Further assume that the rendering algorithm is unbiased, i.e., $\mathbb{E}_{\hat{\mathbf{I}}|\mathbf{X}}[\hat{\mathbf{I}}] = \mathbf{I}(\mathbf{X})$. In this case, the following equality holds, i.e., the gradient estimates are unbiased:*

$$\mathbb{E}_{\hat{\mathbf{I}}|\mathbf{X}}\left[\nabla_\theta \|\varphi_\theta(\mathbf{X}) - \hat{\mathbf{I}}\|^2\right] = \nabla_\theta \|\varphi_\theta(\mathbf{X}) - \mathbf{I}(\mathbf{X})\|^2 \tag{3}$$

Proof. Since the expectation does not depend on the parameters θ, the gradient can be pulled out of the expectation. The left side of Eq. (3) becomes

$$\mathbb{E}_{\hat{\mathbf{I}}|\mathbf{X}}\left[\nabla_\theta \|\varphi_\theta(\mathbf{X}) - \hat{\mathbf{I}}\|^2\right] = \nabla_\theta \mathbb{E}_{\hat{\mathbf{I}}|\mathbf{X}}\left[\|\varphi_\theta(\mathbf{X}) - \hat{\mathbf{I}}\|^2\right] \tag{4}$$

By applying the binomial theorem and the property of the estimator $\hat{\mathbf{I}}$ being unbiased, which means that $\mathbb{E}_{\hat{\mathbf{I}}|\mathbf{X}}\left[\hat{\mathbf{I}}\right] = \mathbf{I}(\mathbf{X})$, the expectation term can be further expanded to

$$\begin{aligned}
\mathbb{E}_{\hat{\mathbf{I}}|\mathbf{X}}\left[\|\varphi_\theta(\mathbf{X}) - \hat{\mathbf{I}}\|^2\right] &= \mathbb{E}_{\hat{\mathbf{I}}|\mathbf{X}}\left[\|\varphi_\theta(\mathbf{X})\|^2 - 2\langle\varphi_\theta(\mathbf{X}), \hat{\mathbf{I}}\rangle + \|\hat{\mathbf{I}}\|^2\right] &(5)\\
&= \mathbb{E}_{\hat{\mathbf{I}}|\mathbf{X}}\left[\|\varphi_\theta(\mathbf{X})\|^2\right] - 2\,\mathbb{E}_{\hat{\mathbf{I}}|\mathbf{X}}\left[\langle\varphi_\theta(\mathbf{X}), \hat{\mathbf{I}}\rangle\right] + \mathbb{E}_{\hat{\mathbf{I}}|\mathbf{X}}\left[\|\hat{\mathbf{I}}\|^2\right] &(6)\\
&= \|\varphi_\theta(\mathbf{X})\|^2 - 2\,\langle\varphi_\theta(\mathbf{X}), \mathbf{I}(\mathbf{X})\rangle + \mathbb{E}_{\hat{\mathbf{I}}|\mathbf{X}}\left[\|\hat{\mathbf{I}}\|^2\right] &(7)
\end{aligned}$$

Taking the gradient with respect to θ in Eq. (7) allows for removing or adding terms that are constant with respect to θ. Thus,

[1] https://pytorch.org

we can replace $\mathbb{E}_{\hat{\mathbf{I}}|\mathbf{X}}\left[\|\hat{\mathbf{I}}\|^2\right]$ with $\|\mathbf{I}(\mathbf{X})\|^2$:

$$\nabla_\theta \mathbb{E}_{\hat{\mathbf{I}}|\mathbf{X}}\left[\|\varphi_\theta(\mathbf{X}) - \hat{\mathbf{I}}\|^2\right] = \nabla_\theta \left[\|\varphi_\theta(\mathbf{X})\|^2 - 2\left\langle \varphi_\theta(\mathbf{X}), \mathbf{I}(\mathbf{X})\right\rangle + \mathbb{E}_{\hat{\mathbf{I}}|\mathbf{X}}\left[\|\hat{\mathbf{I}}\|^2\right]\right] \tag{8}$$

$$= \nabla_\theta \left[\|\varphi_\theta(\mathbf{X})\|^2 - 2\left\langle \varphi_\theta(\mathbf{X}), \mathbf{I}(\mathbf{X})\right\rangle + \|\mathbf{I}(\mathbf{X})\|^2\right] \tag{9}$$

$$= \nabla_\theta \|\varphi_\theta(\mathbf{X}) - \mathbf{I}(\mathbf{X})\|^2 \tag{10}$$

Inserting this into Eq. (4) results in Eq. (3), concluding the proof. □

4. Additional Results

We tested our model on two additional challenging static scenes, with results shown in Fig. 3 and Fig. 4, respectively. For this experiment, we used a realistic bathroom scene and a realistic kitchen scene [1] at an image resolution of 256×256 pixels. Both scenes were trained with a batch size of 128 for 150,000 iterations. Although there is no light transport to be learned in these static scene experiments, we find that our model is able to encode realistic static scenes well, and renders novel views accurately.

For dynamic scenes we also conducted two experiments: one where we compared our approach to a set of baselines in Section 4.2.1 of the main paper, using a dataset with dynamic objects and fixed lights, where we translated and removed objects randomly. And another experiment where we highlight the importance of the Light Transport Layer and the additional photon architecture in Section 4.2.2, on a dataset with dynamic objects and dynamic lights, where we additionally translate rectangular light sources randomly along the ceiling. Tab. 1 shows the full quantitative evaluation of the experiments for dynamic objects and fixed lights. For the experiment with dynamic objects and dynamic lights we provide a full quantitative evaluation in Tab. 2.

Fig. 6 shows additional visual results for the baseline comparison for dynamic objects and fixed lights, complementing Fig. 5 of the main paper. In Fig. 7 we show examples where our method does not predict the illumination accurately. These error images also show that for the denoising approaches errors occur mostly in image regions with high frequency components, i.e. edges and textures. For our approach, errors sometimes also occur in larger image regions when the prediction is inaccurate or sparse. This also explains that while our approach performs best for most of the metrics in Tab. 1 and Tab. 2, the MSE is lower for the denoising approaches.

We show some additional failure cases for dynamic objects and dynamic lights in Fig. 8.

In addition to the quantitative comparison for dynamic objects and fixed lights, we show a more comprehensive quantitative comparison for dynamic objects and dynamic lights in Fig. 5. In addition to MSSIM and FID, we compare L1 feature losses from different stages of the Inception v3 network [11, 12], showing that our approach clearly outperforms the denoising baselines on different levels of image abstraction.

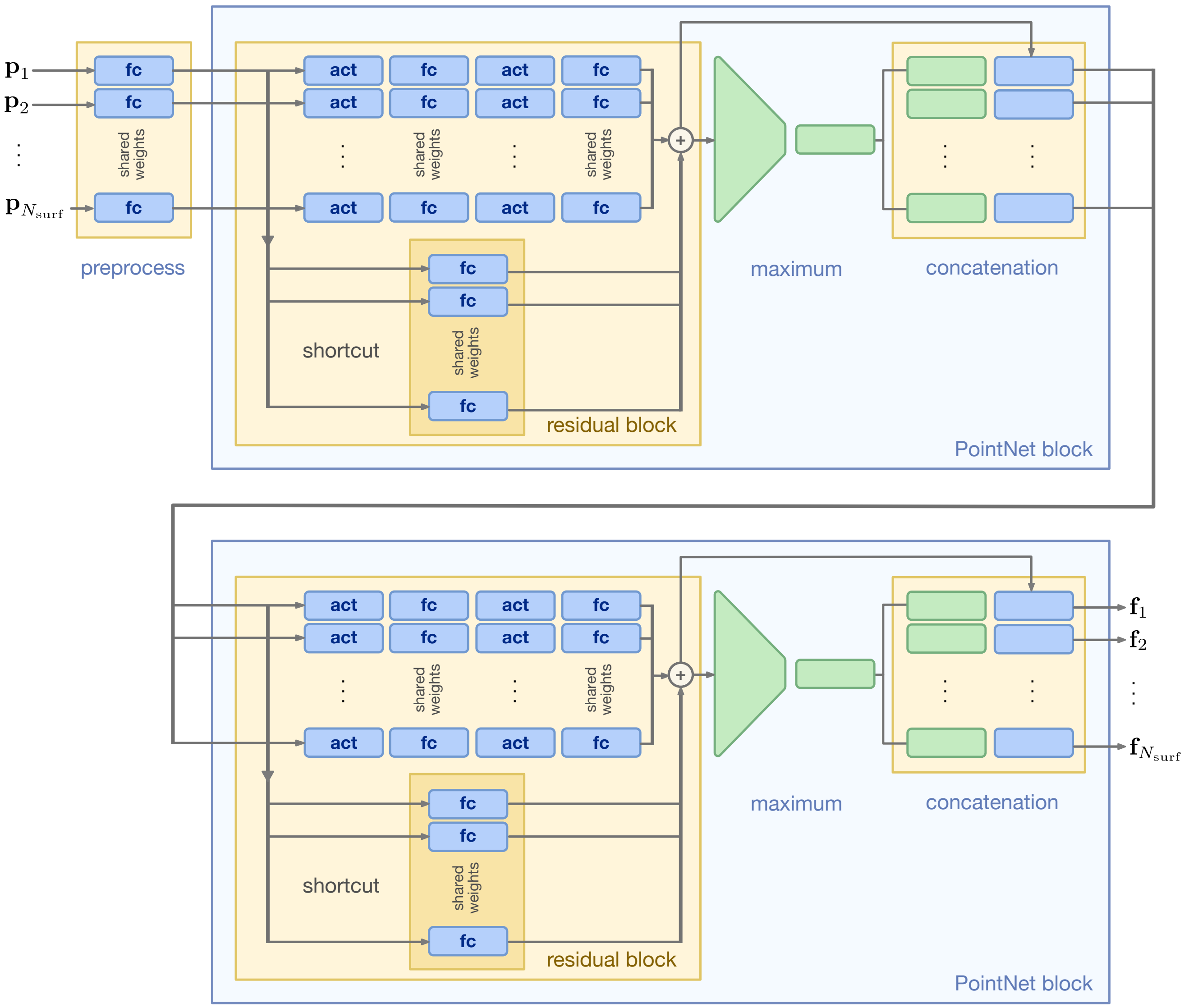

Figure 1. **Light Transport Layer.** In the first stage of the Light Transport Layer all points and supplementary point information $\mathbf{p}_i$ are processed in a preprocessing layer, whose purpose is to align its output feature dimension with the input feature dimension of the PointNet block. The point features are then processed in two consecutive PointNet blocks. A PointNet block comprises a residual block, where local features are computed for each point. The fully connected layers (hidden, output and shortcut layers) consist of 32 output neurons each, where the weights within one layer are shared between the input points. The input dimension to the first fully connected layer in a residual block is aligned with the output dimension of a PointNet block (64). Therefore, a fully connected shortcut layer is required for matching the feature dimensions at the end of a residual block. Following the residual block within a PointNet block, point features are concatenated with a global feature, which is computed as the maximum feature vector of all local features. The output features of the second PointNet block are denoted by $\mathbf{f}_i$. We denote fully connected layers by **fc** and ReLU activation functions by **act**.

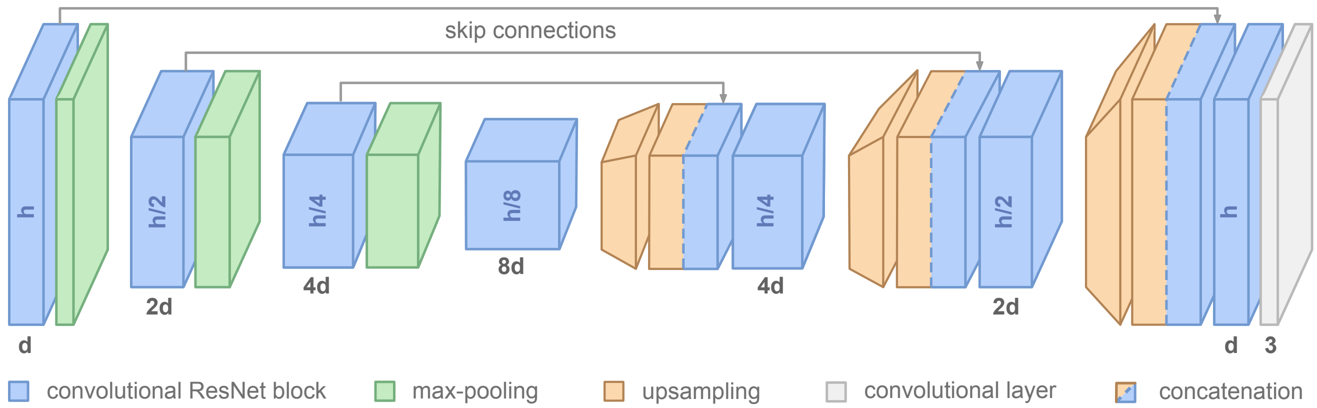

Figure 2. **Image Synthesis Layer.** For final image synthesis we use a UNet [10] architecture where the resolution is reduced in three steps and expanded again. To this end, each level comprises a convolutional ResNet [2] block consisting of two 3×3 convolutional layers and ReLu activations. We use the same feature dimension for the input, hidden and output layers in a convolutional ResNet block. The convolutional ResNet blocks are followed by a downsampling step, which is implemented using max-pooling layers. The feature dimension of the convolutional layers depend on the level, starting at a dimension of $d = 64$, which is then doubled after each downsampling step. The features of the lowest level are then upsampled again using bilinear interpolation, concatenated with the convolutional ResNet block output from the respective downsampling layer through a skip connection and processed in another convolutional ResNet block. After the last upsampling layer an additional convolutional layer is used to render an image with three channels. The numbers below the layers correspond to the number of feature maps in each layer. The numbers inside the layers correspond to the layer's resolution, starting at a square resolution of $h \times h$. We use $h = 128$ in our static scene ablation study and $h = 256$ for the other experiments.

Figure 3. **Bathroom Scene.** Results of our model on a realistic static bathroom scene.

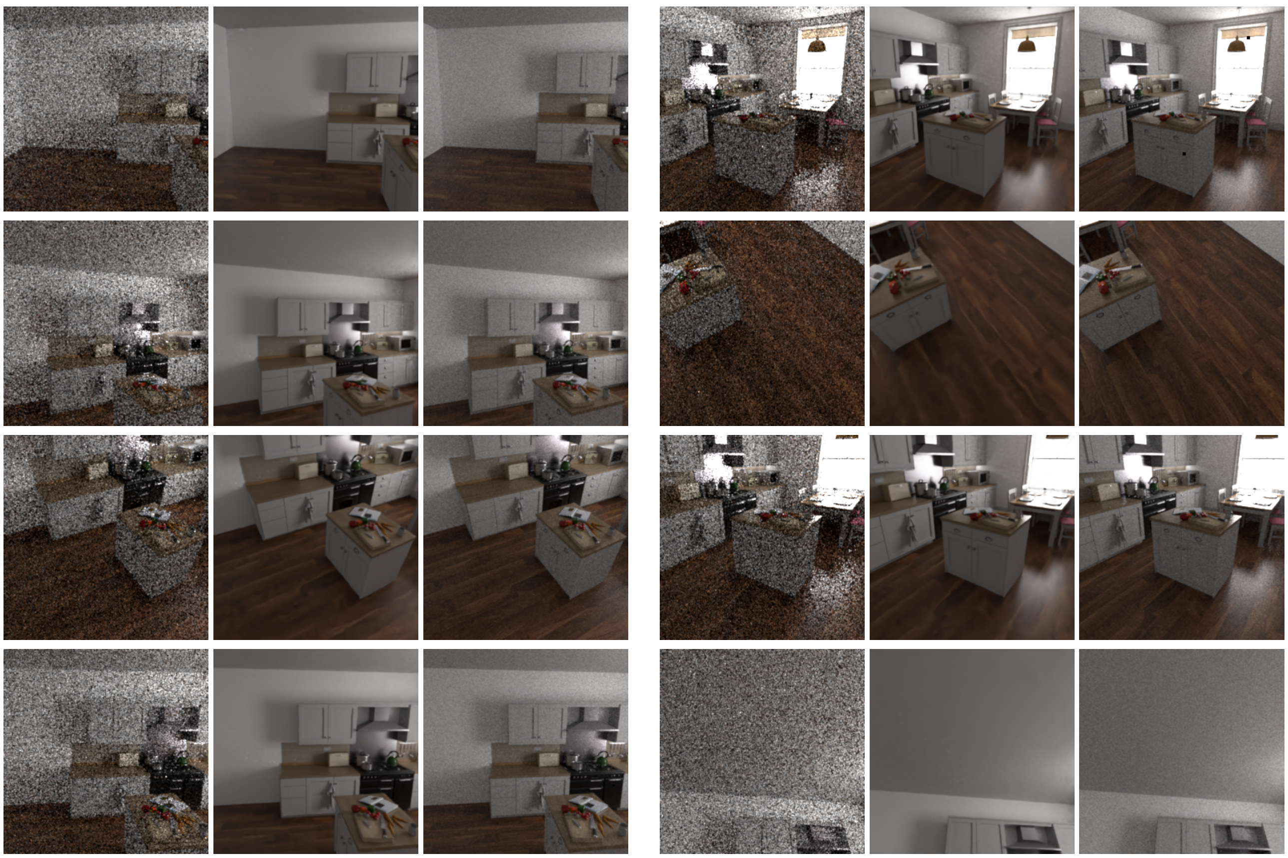

Figure 4. **Kitchen Scene.** Results of our model on a realistic static kitchen scene.

Architecture	time / frame	MSE	MSSIM	FID	Feature L1
Denoising (1/1)	1.5059s	0.0005	0.880	26.4	0.163
Denoising (1/4)	0.3800s	0.0007	0.867	28.1	0.172
Denoising (1/16)	0.0986s	0.0012	0.835	38.7	0.203
Denoising (1/32)	0.0532s	0.0018	0.813	54.1	0.233
Denoising (1/64)	0.0283s	0.0029	0.781	94.0	0.281
CNN only	0.0191s	0.0043	0.835	36.1	0.195
Feature projection	0.0210s	0.0037	0.841	32.5	0.185
Ours (w/o photons)	0.0243s	0.0044	0.841	31.4	0.184
Ours (w/ photons)	0.0459s	0.0028	0.849	30.6	0.182

Table 1. **Dynamic Objects and Fixed Lights.** Quantitative evaluation for our experiment on dynamic objects and fixed lights.

Architecture	time / frame	MSE	MSSIM	FID	Feature L1
Denoising (1/1)	1.5059s	0.0002	0.930	17.1	0.137
Denoising (1/4)	0.3801s	0.0002	0.923	17.6	0.143
Denoising (1/16)	0.0988s	0.0005	0.896	23.5	0.172
Denoising (1/32)	0.0518s	0.0008	0.874	38.6	0.207
Denoising (1/64)	0.0283s	0.0016	0.839	84.1	0.269
CNN only	0.0190s	0.0100	0.827	33.7	0.199
Feature projection	0.0208s	0.0098	0.827	32.9	0.197
Ours (w/o photons)	0.0243s	0.0029	0.871	30.0	0.184
Ours (w/ photons)	0.0468s	0.0014	0.887	25.1	0.172

Table 2. **Dynamic Objects and Dynamic Lights.** Quantitative evaluation for our experiment on dynamic objects and dynamic lights.

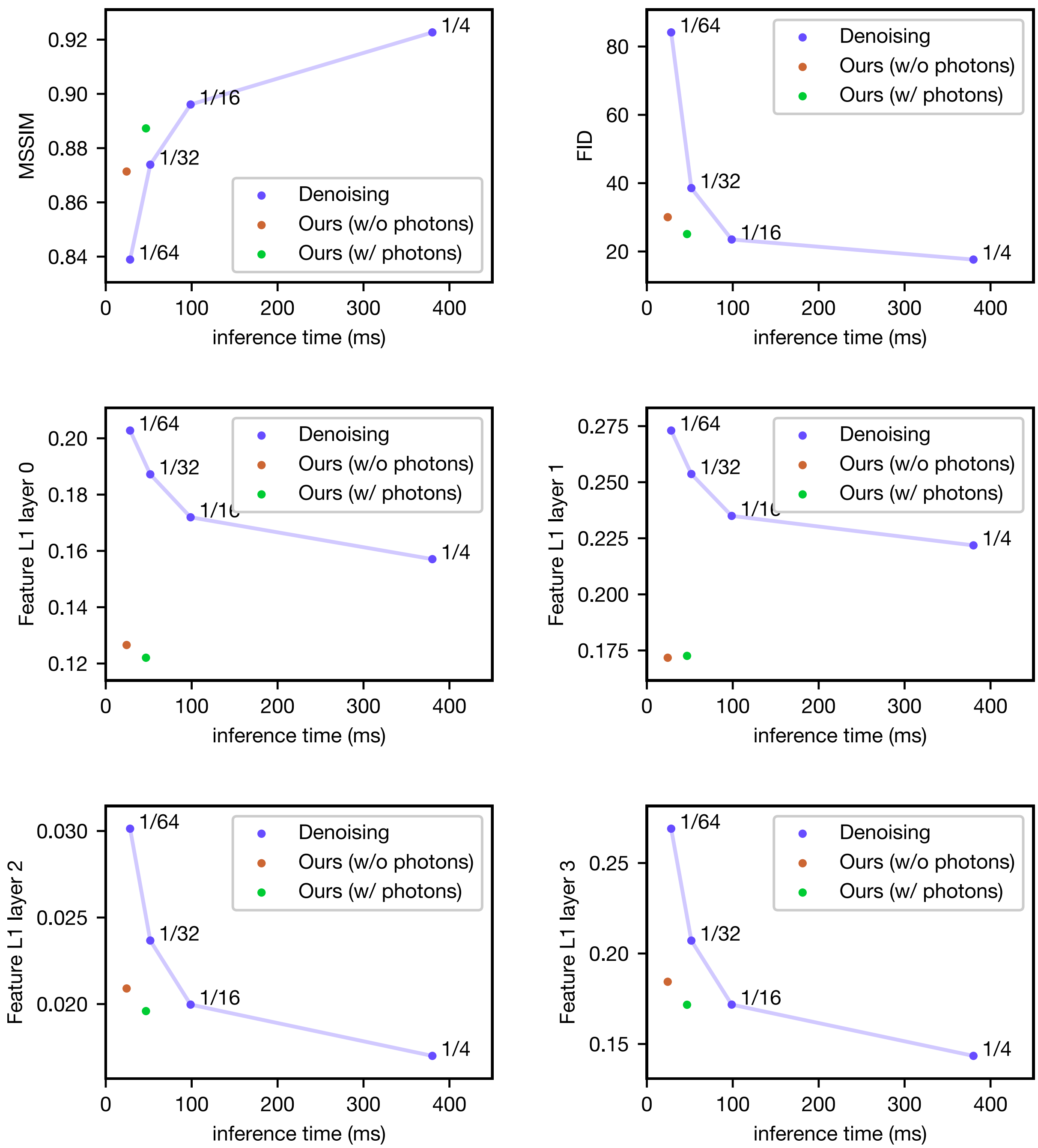

Figure 5. **Dynamic Objects and Dynamic Lights.** This plot shows a quantitative comparison of our approach with the denoising baseline for different sample densities. We plot reconstruction accuracy over inference time for our experiment on dynamic objects and dynamic lights. The denoising labels refer to the ratio of pixels that are dropped. The layer indices (0–3) for the Feature L1 losses refer to outputs of the four major layers in the Inception v3 network.

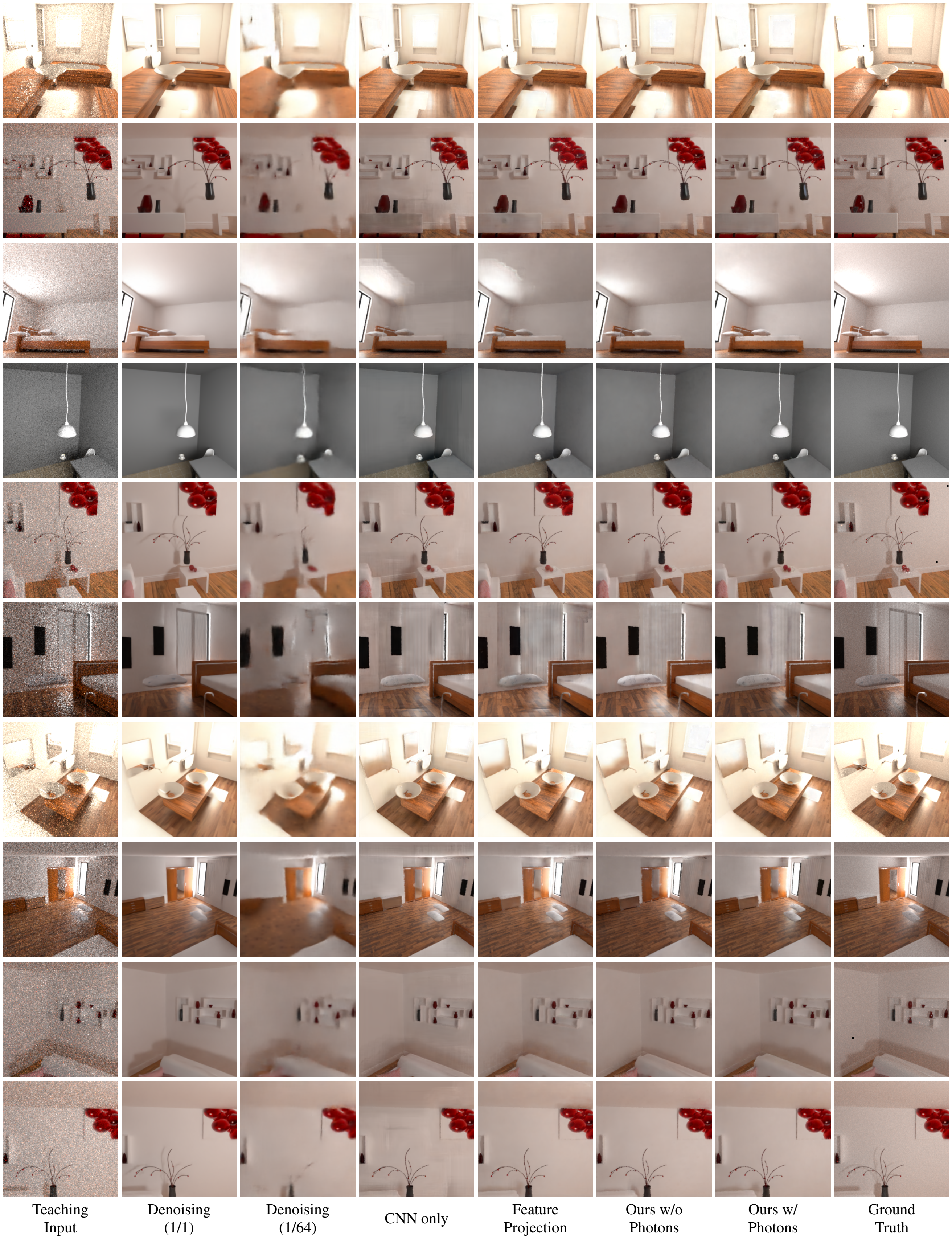

Figure 6. **Dynamic Objects and Fixed Lights.** Additional results for our method as well as for the baselines for dynamic objects and fixed lights, complementing Fig. 5 of the main paper.

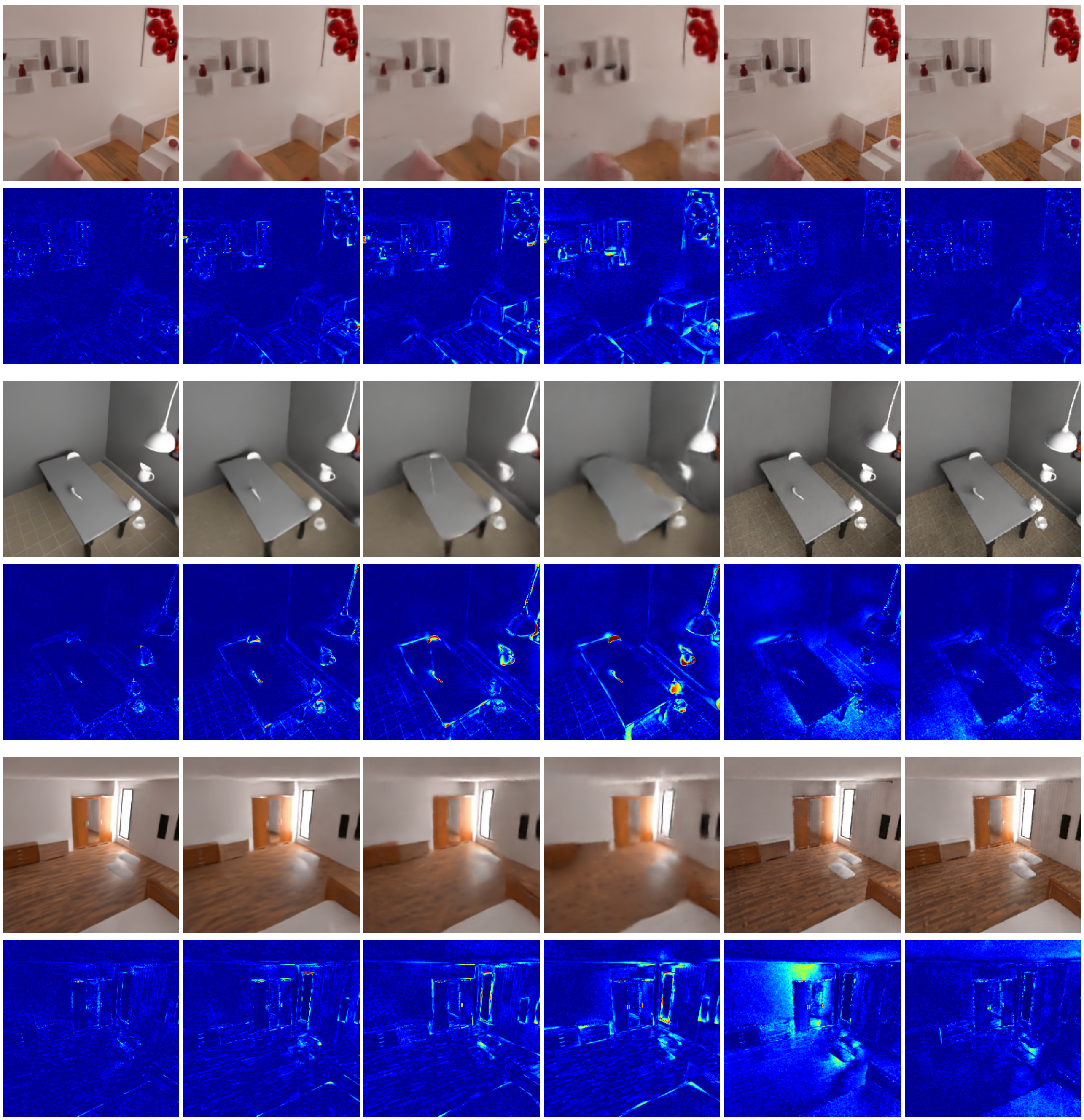

Denoising (1/4) Denoising (1/16) Denoising (1/32) Denoising (1/64) Ours w/o photons Ours w/ photons

Figure 7. **Dynamic Objects and Fixed Lights.** Predictions and error images with respect to ground truth for different denoising approaches and our approach for dynamic objects and fixed lights. Error plots are shown below the respective prediction.

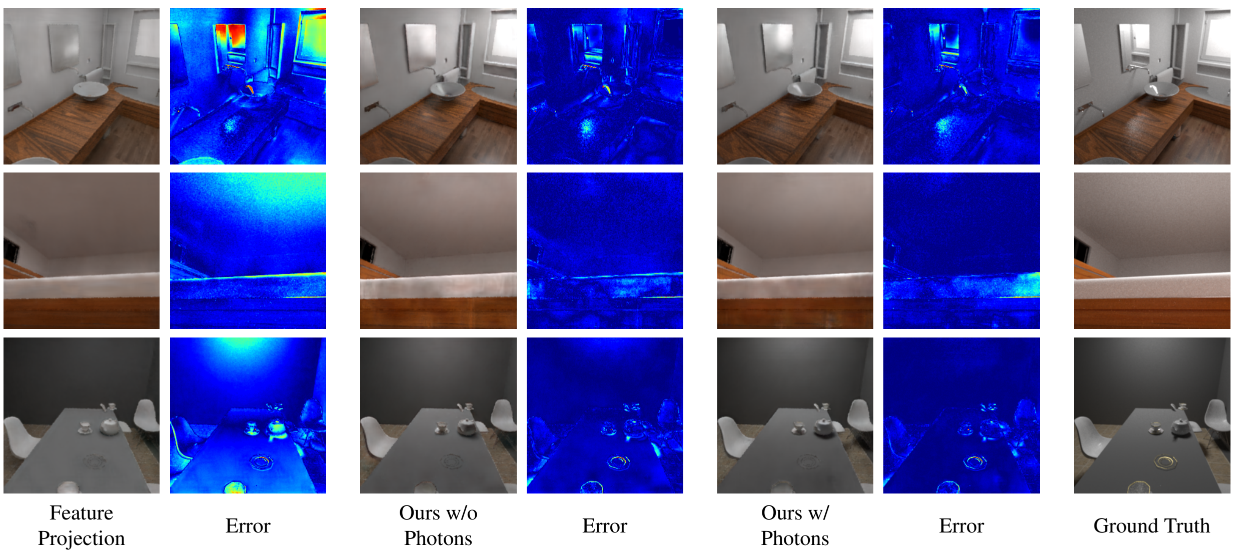

Figure 8. **Dynamic Objects and Dynamic Lights.** Example scenarios that are challenging for our approach with dynamic objects and dynamic lights. We observe failure cases for specular materials and mirrors, when objects are close to the camera and in the presence of fine shadows.

References

[1] Benedikt Bitterli. Rendering resources, 2016. https://benedikt-bitterli.me/resources/. 2, 4

[2] Kaiming He, Xiangyu Zhang, Shaoqing Ren, and Jian Sun. Deep residual learning for image recognition. In *Proc. IEEE Conf. on Computer Vision and Pattern Recognition (CVPR)*, 2016. 1, 6

[3] Wenzel Jakob. Mitsuba renderer, 2010. http://www.mitsuba-renderer.org. 3

[4] Diederik P. Kingma and Jimmy Ba. Adam: A method for stochastic optimization. In *Proc. of the International Conf. on Learning Representations (ICLR)*, 2015. 3

[5] Alexander Krull, Tim-Oliver Buchholz, and Florian Jug. Noise2void - learning denoising from single noisy images. In *Proc. IEEE Conf. on Computer Vision and Pattern Recognition (CVPR)*, 2019. 3

[6] Eric P Lafortune and Yves D Willems. Bi-directional path tracing. 1993. 3

[7] Jaakko Lehtinen, Jacob Munkberg, Jon Hasselgren, Samuli Laine, Tero Karras, Miika Aittala, and Timo Aila. Noise2noise: Learning image restoration without clean data. In *Proc. of the International Conf. on Machine learning (ICML)*, 2018. 3

[8] Adam Paszke, Sam Gross, Soumith Chintala, Gregory Chanan, Edward Yang, Zachary DeVito, Zeming Lin, Alban Desmaison, Luca Antiga, and Adam Lerer. Automatic differentiation in PyTorch. In *NIPS Autodiff Workshop*, 2017. 3

[9] Charles R Qi, Hao Su, Kaichun Mo, and Leonidas J Guibas. Pointnet: Deep learning on point sets for 3d classification and segmentation. In *Proc. IEEE Conf. on Computer Vision and Pattern Recognition (CVPR)*, 2017. 1

[10] Olaf Ronneberger, Philipp Fischer, and Thomas Brox. U-net: Convolutional networks for biomedical image segmentation. In *Medical Image Computing and Computer-Assisted Intervention (MICCAI)*, 2015. 6

[11] Christian Szegedy, Wei Liu, Yangqing Jia, Pierre Sermanet, Scott E. Reed, Dragomir Anguelov, Dumitru Erhan, Vincent Vanhoucke, and Andrew Rabinovich. Going deeper with convolutions. In *Proc. IEEE Conf. on Computer Vision and Pattern Recognition (CVPR)*, 2015. 4

[12] Christian Szegedy, Vincent Vanhoucke, Sergey Ioffe, Jonathon Shlens, and Zbigniew Wojna. Rethinking the inception architecture for computer vision. In *Proc. IEEE Conf. on Computer Vision and Pattern Recognition (CVPR)*, 2016. 4